nature portfolio

https://doi.org/10.1038/s41567-022-01599-8

Supplementary information

Gap solitons in a one-dimensional driven-dissipative topological lattice

In the format provided by the authors and unedited

Supplementary materials for the paper entitled: Gap solitons in a 1D driven-dissipative topological lattice

N. Pernet[1], P. St-Jean[1]*, D.D. Solnyshkov[2,3], G. Malpuech[2], N. Carlon Zambon[1], Q. Fontaine[1], B. Real[4], O. Jamadi[4], A. Lemaître[1], M. Morassi[1], L. Le Gratiet[1], T. Baptiste[1], A. Harouri[1], I. Sagnes[1], A. Amo[4], S. Ravets[1], J. Bloch[1]

[1]*Université Paris-Saclay, CNRS, Centre de Nanosciences et de Nanotechnologies (C2N), 91120, Palaiseau, France*

[2]*Institut Pascal, PHOTON-N2, Université Clermont Auvergne, CNRS, SIGMA Clermont, F-63000 Clermont-Ferrand, France.*

[3]*Institut Universitaire de France (IUF), 75231 Paris, France*

[4]*Université de Lille, CNRS, Laboratoire de Physique des Lasers Atomes et Molécules (PhLAM), 59000 Lille, France*

1 Experimental determination of the polariton parameters

To estimate the Rabi splitting characterizing the exciton photon coupling in our cavity sample, we measure angularly resolved photoluminescence on a planar part of our cavity. To do so, we probe a large square pillar of $70\,\mu\mathrm{m}$ x $100\,\mu\mathrm{m}$, which can be considered as 2D when looking at regions far from its edges. The measured polariton dispersions are presented in Fig.S1(a). They are well reproduced using a $3.20\,\mathrm{meV}$ Rabi splitting.

*These authors contributed equally: N. Pernet, P. St-Jean

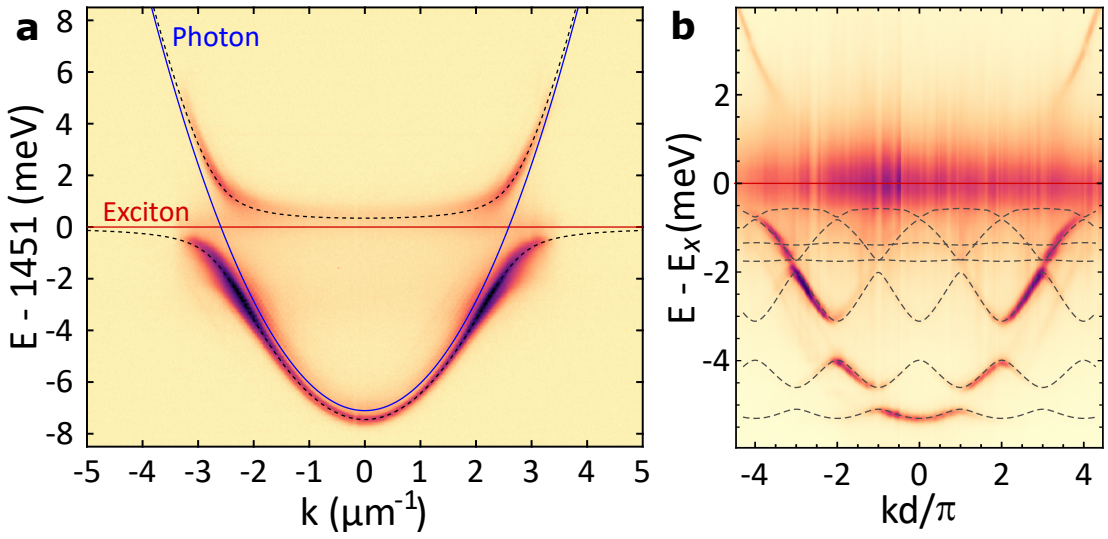

Figure S1: a) Spectrally resolved photoluminescence intensity as a function of momentum k measured under non resonant excitation on the planar cavity. The blue (red) line shows the extracted dispersion of the uncoupled cavity mode (quantum-well exciton). Dashed grey lines show the simulated dispersion using a $3.20\,\mathrm{meV}$ Rabi splitting. b) Spectrally resolved photoluminescence intensity as a function of momentum k measured on the SSH polariton lattice. The red line shows the exciton energy. Dashed grey lines are simulated dispersions obtained solving a 2D Schrödinger equation.

Angularly resolved photoluminescence measured on the polariton SSH lattice is presented in Fig.S1(a). Note that Fig.1b of the main text presents the same data but zoomed on a smaller energy scale. One can see higher-energy bands emerging from hybridization of the p modes, the exciton line as well as part of the upper branch.

In order to reproduce the dispersion relation we solve the 2D optical Schrödinger equation for the transverse modes of the system. Indeed, within a paraxial approximation, the coupled micropillars can be regarded as infinite overlapping waveguides presenting an effective refractive index $n_{\text{eff}} \approx 3.3$. In the kinetic term, the effective mass of the photon is given by the relation $m_c^* = E_0 n_{\text{eff}}^2/c^2 \approx 3 \cdot 10^{-5} m_e$ where $E_0 \approx 1.45$ eV is the 2D cavity mode energy at normal incidence. The potential term is given by $U(x,y) = \frac{E_0}{2}\frac{n_{\text{eff}}^2 - n^2(x,y)}{n_{\text{eff}}^2}$, yielding zero in the pillars and $U_0 \approx 0.65$ eV elsewhere. Given the translational invariance of the system along x, one can impose periodic boundary conditions at the edge of the unit cell and diagonalize the discretized Hamiltonian operator to find the frequency and envelope of the Bloch waves as a function of the wavevector k_x. We then introduce the strong coupling regime between the photon modes and the exciton considering a $3.20\,\text{meV}$ Rabi splitting. The simulated band structure nicely reproduces the experimental results (see Fig.S1(b)), using as a fitting parameter a -4.9 meV detuning between the lowest energy photon mode of the pillar lattice and the exciton.

2 Real space photoluminescence spectra for the two polariton lattices presented in Fig.1

To complement the photoluminescence experiments described in Fig.1 of the main text we present, in Fig.S2, spatially resolved measurements corresponding to panels 1b and 1d of the main text. We clearly evidence that the additional state observed in the gap on panel 1d is highly localized on the interface pillar with sublattice polarized tails on each side (see right panel of Fig.S2). This further confirms that this state is a topological interface state.

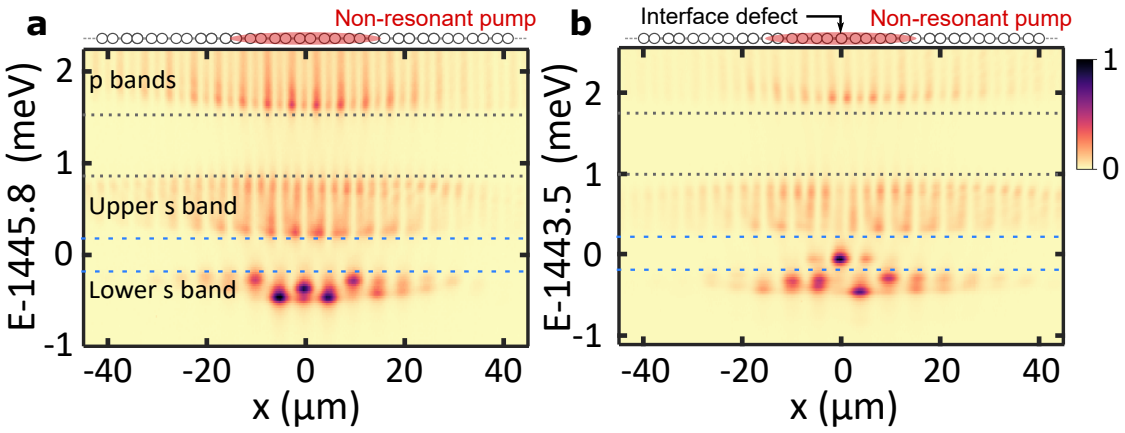

Figure S2: Spatially resolved emission a function of the energy measured under off resonant excitation a) on an homogeneous lattice, b) when the excitation spot (schematically shown on top of both panels) overlap with an engineered interface defect.

3 The optical bistability associated to the formation of driven-dissipative solitons

We provide additional data showing that bistable behaviour and hysteresis cycles are associated to each of the two nonlinear thresholds described in Fig.2b of the main text. This well-known effect, ubiquitous in nonlinear systems, has its origin in the interplay between drive, loss and the Kerr

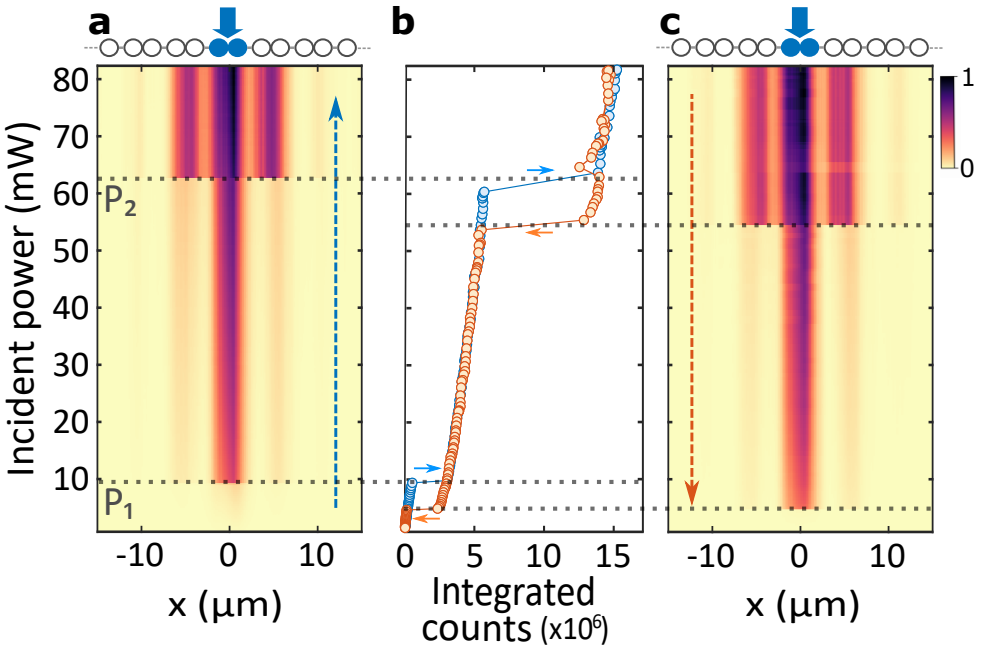

Figure S3: **a,** Spatially resolved intensity profiles, integrated along the direction perpendicular to the lattice, measured as the driving power is ramped up. The intensity is normalized to its maximum value. The driven dimer is schematically shown on top. **b,** Total integrated intensity measured when scanning the excitation power up (blue) and down (orange). Blue (orange) arrows highlight the nonlinear jumps associated to the formation (extinction) of gap solitons. Horizontal dotted lines delimit the gap soliton bistability regions. **c,** Same as (a) but when the driving power is ramped down.

nonlinearity[1].

Fig. S3 shows the evolution of the intensity profile and the total intensity as we ramp the power up and down. Due to the formation and disappearance of gap solitons, we observe hysteresis cycles in the total intensity (as shown in panel b) delimiting a bistability region in excitation power for the gap soliton.

4 Experimental study of the soliton profiles as a function of the laser energy within the topological gap

We analyse, in this section, three soliton profiles (see Fig. S4(a)) measured for three different values of the laser detunings ΔE. We observe that the spin polarization progressively decreases (the intensity difference between the two sublattice is reduced) when the laser energy departs from the center of the topological gap (going from $\Delta E = -0.04$ meV to $\Delta E = -0.25$ meV). These measurements clearly highlight that the spin polarization of the soliton tails is directly connected to the fact that these solitons lie within the SSH gap.

As expected for gap solitons, note that the exponential decay of the soliton tails becomes more abrupt when the soliton energy approaches the center of the gap.

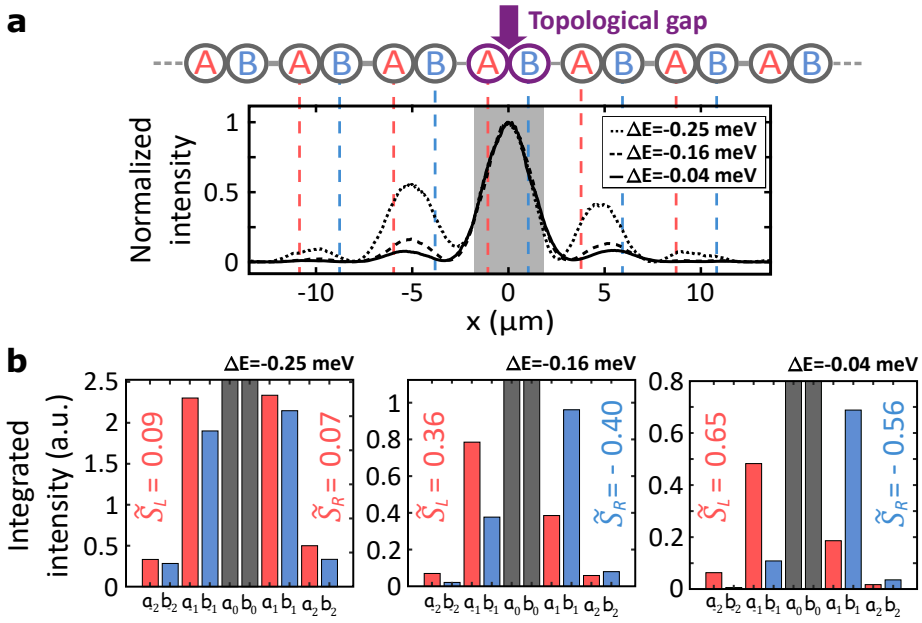

Figure S4: a) Soliton profiles (intensity normalized to the maximum) measured for different energies of the excitation laser $\Delta E = -0.25$ meV (dotted line), $\Delta E = -0.16$ meV (dashed line), and $\Delta E = -0.04$ meV (solide line). Dashed red and blue lines mark the positions of A and B sites. b) Histograms of the intensity integrated around the center of each site. The grey bars corresponding to the soliton core have been cut to better visualize the soliton tails. Bars corresponding to A (resp. B) sites are colored in red (resp. blue).

5 Mapping the nonlinear SSH polariton lattice to a 1D continuous model

The 1D potential. To compute the nonlinear properties of the SSH polariton lattice, we could solve a 2D nonlinear Schrödinger equation. However, all the physics can be captured within a simpler 1D approach based on the definition of an effective 1D potential. The quantization of the polariton modes in the vertical direction makes them massive and allows using a 1D effective Schrödinger equation considering only the propagating direction along the lattice. This approach is numerically lighter than a continuous 2D model, but allows to consistently take into account effects neglected by the tight-binding model such as band-mixing effects and the finite size of the lattice sites. The 1D landscape for the effective potential is constituted by a series of potential wells separated by two types of energy barriers. The strong and weak links are respectively represented by barriers of small and large amplitudes (corresponding to strongly and weakly overlapping pillars), as shown in Fig. S5 (a). The corresponding Hamiltonian therefore reads:

$$\mathcal{H}_0^{(1\mathrm{D})}(x) = \left[-\frac{\hbar^2}{2m}\nabla^2 + V(x)\right] \tag{S1}$$

where m is the polariton mass and $V(x)$ is the aforementioned energy potential.

For convenience, we remind here the time-dependent 1D Gross-Pitaevskii equation (Eq. (3) of the main text) that we use to simulate the experimental results:

$$i\hbar\frac{d\psi(x,t)}{dt} = \mathcal{H}_0^{(1\mathrm{D})}(x)\psi(x,t) + g|\psi(x,t)|^2\psi(x,t) - i\frac{\hbar\gamma}{2}\psi(x,t) + iF(x)e^{-i\omega_p t} \tag{S2}$$

The simulated band structure of the polariton modes in the 1D potential $V(x)$ is obtained by solving this equation without interactions ($g = 0$) for a localized excitation at $t = 0$: $\psi(x,0) =$

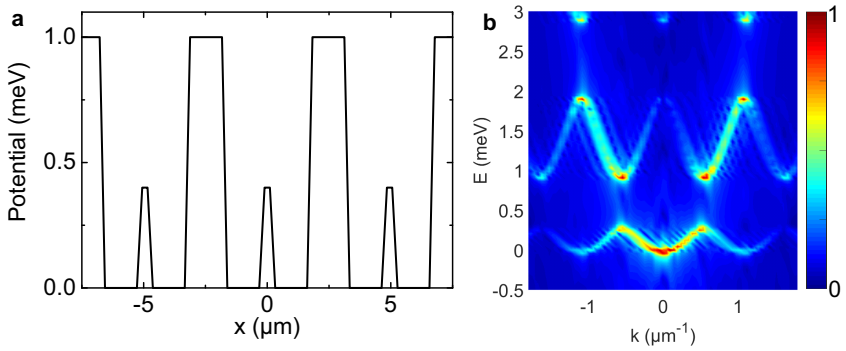

Figure S5: a) Effective 1D potential describing an SSH chain; b) Dispersion obtained in numerical simulations.

$\exp(-x^2/2\sigma^2)$, where the width of the pulse has to be sufficiently small $\sigma = 0.5$ μm. It is represented in Fig. S5 (b) and shows a qualitative agreement with the one obtained experimentally. The size of the gap and the effective mass of the lower band are well reproduced. The differences between the experimental and the simulated bands visible at higher energies are most probably due to the 2D nature of the actual system.

6 Simulation of gap soliton spatial profiles shown in Fig.2 of the main text

Solving Eq. (S2) with the parameters given in Numerical Methods of the main text and with a linear increase of the pumping power determined by $|F|^2$, we obtain the data shown in Fig. S6, which nicely reproduce the experimental observations. In particular, we observe the formation of a 1D dimer soliton above a first threshold, and then above a second threshold the formation of a symmetric three dimer soliton. The simulated profiles shown in Fig. 2 (c-d) of the main text corresponds to powers indicated with dashed horizontal lines.

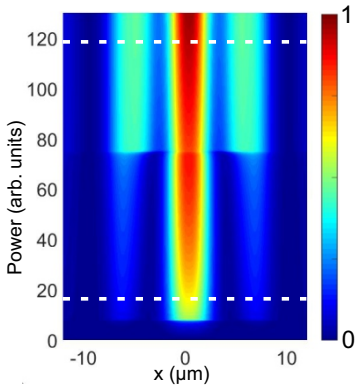

Figure S6: Numerical simulations showing the spatial distribution of the polariton density $|\psi(x)|^2$ at different pumping powers when scanning up the power. Dashed horizontal lines indicate the simulated profiles shown in Fig. 2 (c-d) of the main text.

7 Numerical study of the soliton robustness against a defect induced by an non-resonant pump

Here, we describe the results of numerical simulations, based on Eq. (S2), corresponding to the experimental measurements shown in Fig. 3 (c-g) of the main text. To take into account the optically induced defect, we add to $V(x)$ an additional potential $V_D(x) = (\Delta + i\Gamma)G(x)$, where $G(x)$ is a Gaussian with 3 μm FWHM representing the spot shape. Δ is the defect amplitude measured experimentally on a reference micropillar. Γ is a positive imaginary part describing stimulated scattering from the reservoir into the polariton mode. The amplitude of this imaginary part is calibrated considering the ratio of the pumping power to the threshold power for polariton lasing in the reference micropillar (30% of the lasing threshold power for a 100 μeV blueshift).

The simulated intensity profiles are shown in Fig. S7 (a-e) for the following defect amplitudes

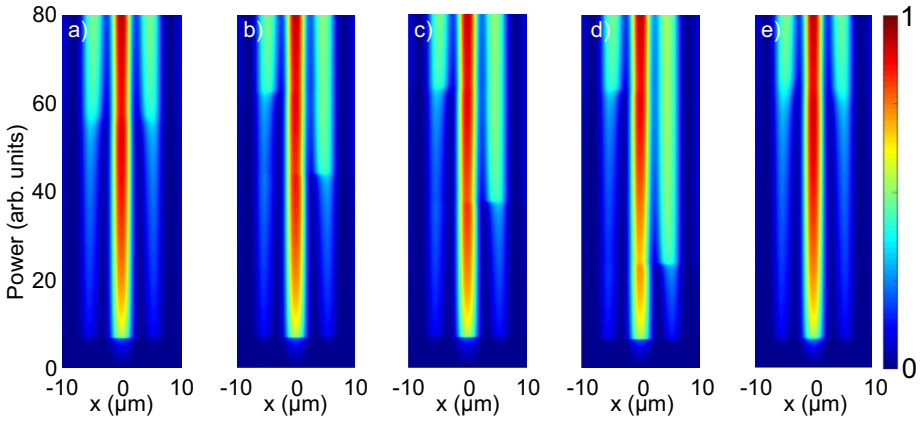

Figure S7: Numerical simulations showing the spatial distribution of the polariton density $|\psi(x)|^2$ at different pumping powers, for the following defect potentials (μeV) a) 0 (B-site), b) 8 (B-site), c) 12 (B-site), d) 20 (B-site), e) 20 (A-site).

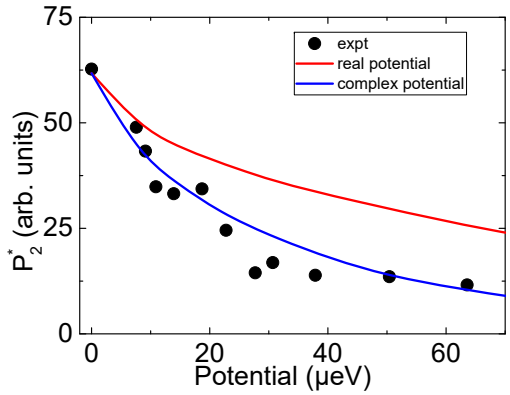

Figure S8: Values of the threshold power P_2^* measured with a defect located on a B site (black dots), simulated taking into account the real part of the defect potential only (red line) or taking into account both its real and imaginary parts (blue line).

(expressed in μeV): 0 (a), 8 (b), 12 (c), 20 on the B-site with high soliton density (d) and 20 on the A-site with low soliton density (e). The calculated profiles show good agreement with the measured ones. To quantitatively compare theory with experiments we report in Fig. S8 the measured values of P_2^* and the simulated values taking into account only the real part of the defect or both real and imaginary parts. We see that the gain leads to a significant reduction of the threshold. The agreement with experiments is better when including both real and imaginary parts of the defect, that is when taking into account the non-Hermitian nature of the defect.

8 Simulation of spin polarized solitons

We discuss here simulation of experiments reported in the last part of the main text. The lattice is resonantly driven with two pumping spots focused on the two pillars composing the central dimer. The pumps have same amplitude but phase difference $\Delta\varphi$. The steady state nonlinear intensity profiles strongly depend on $\Delta\varphi$.

Phase scan and profiles. In this subsection, we show the results of numerical simulations corresponding to the experiment shown in Fig. 4 (a) of the main text. We vary the relative phase $\Delta\varphi$ between the two pumps between 0 and 2π, while keeping the pump intensity constant. Numerical results are presented in Fig. S9. They reproduce the overall experimental behavior with a complex sequence of abrupt switchings between distinct regimes with different numbers of bright pillars (starting from $\Delta\varphi = 0$, we successively observe three bright dimers, two bright dimers, three bright pillars, and only one bright pillar before switching to the linear regime as we approach

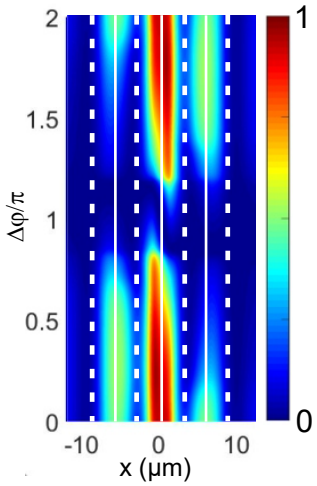

Figure S9: Numerical simulations showing the spatial distribution of the polariton density $|\psi(x)|^2$ as a function of phase difference $\Delta\varphi$ between the two pumping lasers on A and B sites of the same unit cell. Thick vertical dashed lines delimits the dimers, while thin solid lines mark their center.

$\Delta\varphi = \pi$). Interestingly, the simulations reproduce the establishment of nonlinear solutions with non-zero global spin polarization: In the vicinity of $\Delta\varphi = \pi$, we obtain a highly spin polarized soliton, with a single bright pillar and a profile similar to a topological edge state of a SSH model.

Note that for these simulations, we have used the pump power as a fitting parameter. We have selected a value that reproduces best the experimental results, approximately equivalent to 40 mW, with three dimers in the high density regime at $\Delta\varphi = 0$. Changing this intensity affects the phase threshold close to $\Delta\varphi = \pi$ and modifies the level of asymmetry in the intensity spatial distribution.

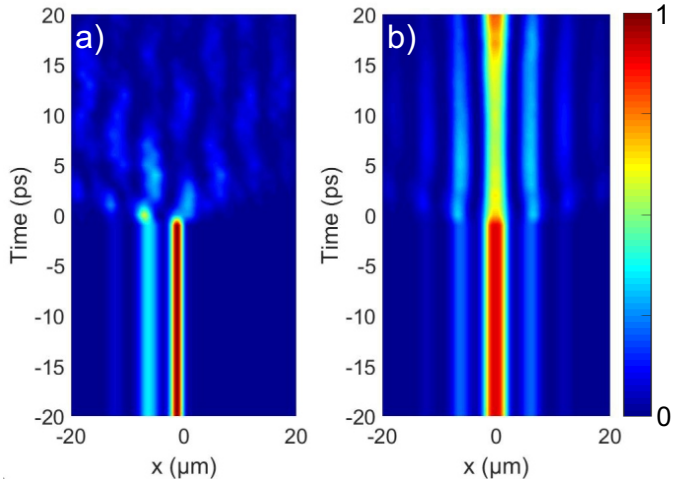

Figure S10: Numerical simulations showing the spatial distribution of the polariton density $|\psi(x)|^2$ as a function of time. The pumping and decay terms are artificially turned off at $t = 0$. a) asymmetric configuration with $\Delta\varphi = 0.94\,\pi$ (corresponding to Fig. 4 of the main text) is unstable; b) symmetric configuration is close to the conservative gap soliton and remains relatively stable, only exhibiting oscillations.

Stability of the spin polarized solitons in absence of drive and dissipation. The strongly asymmetric solutions observed for a phase difference $\Delta\varphi \approx \pi$ can only be obtained thanks to the driven-dissipative polariton configuration that we use. This is a very important difference with an ordinary topological gap soliton, which can be studied in a conservative system, such as optical waveguides arrays. In this section, we illustrate numerically this property by monitoring the time evolution of the system after we abruptly switch off drive and dissipation in Eq. (S2). As shown in Fig. S10(a), the asymmetric spin polarized soliton, obtained for $\Delta\varphi$ close to π, is not a stationary solution any more. Moreover, being far from any stationary solution, it decays very rapidly. To

provide a comparison, we also show a simulation for $\Delta\varphi = 0$, in which case the solution is much closer to a conservative topological gap soliton (although the central part in the bistable regime has a higher density than that expected in the conservative case). Panel (b) shows that in such a case, the solution does not evolve much: it exhibits weak oscillations around the stationary solution (which is a topological gap soliton). This is especially visible in the periodic variation of the central dimer density.

9 Tight-binding analytic expressions of the soliton wavefunction

We provide here an analytical derivation of the soliton profiles reported in our work within the framework of the tight-binding approach. We write the Gross Pitaevskii equation for an infinite 1D chain. In the rotating frame at the pump frequency ω, and using the formalism introduced in the main text, we get:

$$-\Delta E\, b_n - J' a_{n+1} - J a_n + g_n |b_n|^2 b_n - i\frac{\gamma}{2} b_n + i F_{b,n} = 0 \tag{S3}$$

$$-\Delta E\, a_n - J' b_{n-1} - J b_n + g_n |a_n|^2 a_n - i\frac{\gamma}{2} a_n + i F_{a,n} = 0 \tag{S4}$$

We recall that ΔE is the energy detuning between the pump and the center of the gap. To reproduce the quasi-resonant excitation schemes described in the main text, we set non zero values of the pump amplitudes $F_{a,n}$ and $F_{b,n}$ for unit cell $n = 0$ only. Also, the frequency of the pump is set to the center of the topological gap ($\Delta E = 0$). We then look for solitonic solutions localized on

one dimer (the nonlinearity g_n is non-zero for $n = 0$ only) and with sublattice lattice polarization on both tails ($a_n = 0$ for $n > 0$ and $b_n = 0$ for $n < 0$). For unit cell $n = 0$, we obtain:

$$-Ja_0 + g|b_0|^2 b_0 - i\frac{\gamma}{2} b_0 + iF_0^B = 0 \tag{S5}$$

$$-Jb_0 + g|a_0|^2 a_0 - i\frac{\gamma}{2} a_0 + iF_0^A = 0 \tag{S6}$$

Solving these two coupled nonlinear equation, we determine the values of b_0 and a_0.

To determine the values of b_n for $n > 0$, we first write Eq. S4 for $n = 1$:

$$-J'b_0 - Jb_1 = 0 \tag{S7}$$

By iteration we then get : $b_n = \left(-\frac{J'}{J}\right)^n b_0$ for any value of $n > 0$. The same reasoning yields: $a_n = \left(-\frac{J'}{J}\right)^{|n|} a_0$ for any value of $n < 0$.

For the symmetric pumping scheme, $F_A = F_B$ so that $a_0 = b_0$. As a result, we find two symmetric exponentially decaying tails with full spin polarization. The situation is different when $F_A = F_B e^{i\varphi}$ ($\delta\varphi \gtrsim \pi$). Solving the two coupled equations Eq. S5 and Eq. S6 one finds, in the nonlinear regime ($g_0|a_0|^2 > J$), that a destructive interference may occur and lead to $|a_0|^2 \gg |b_0|^2$. In that case, the resulting solution presents a fully spin polarized tail on the A side, while the soliton tail vanishes on the B side. For $\varphi = \pi$, either a_0 or b_0 is equal to zero (symmetry breaking). The resulting solution presents zero amplitude on one side and a fully spin polarized exponential tail on the other side. This is precisely the same profile as the profile of a linear edge state[2].

10 References

1. In Gibbs, H. M. (ed.) *Optical Bistability: Controlling Light with Light* (Academic Press, 1985). URL https://doi.org/10.1016/B978-0-12-281940-7.50003-2.

2. Kunst, F. K., van Miert, G. & Bergholtz, E. J. Lattice models with exactly solvable topological hinge and corner states. *Phys. Rev. B* **97**, 241405 (2018).